AIAA JOURNAL
Vol. 47, No. 6, June 2009

Hybrid Empirical/Computational Aeroacoustics Methodology for Rocket Noise Modeling

Damiano Casalino* and Mattia Barbarino†
Italian Aerospace Research Center, I-81043 Capua, Italy
Mariano Genito‡
European Launch Vehicle, S.p.A., I-00034 Colleferro, Italy
and
Valerio Ferrara§
Avio S.p.A., I-00034 Colleferro, Italy

DOI: 10.2514/1.38634

Sound pressure level contours and spectral sound distributions around the Vega launch system are computed by means of a standard empirical model developed by NASA and a novel hybrid empirical/computational aeroacoustics approach. The empirical prediction is validated against available noise spectra measured on a scaled mock-up, showing a fairly good agreement when standard values for the model constants are used. The jet sources employed in the empirical prediction are then used to convolute a database of tailored Green's functions computed by means of a frequency-domain computational aeroacoustics code. This second approach allows the consideration of the real launch pad geometry and, in the limit of the grid resolution drawn by the acoustic wavelength, the mean flow refraction effects in the jet stream. The mean flow is supplied by a FLUENT simulation and projected onto the computational aeroacoustics grid. This is a Cartesian grid generated automatically and used in connection with an immersed-boundary approach. It is shown that the hybrid empirical/computational aeroacoustics prediction is able to explain some discrepancies observed between the experimental data and the empirical predictions. In addition, it generates a basis of elementary fields to be used in a source localization method under development in the framework of the Innovative Aerothermodynamic Configurations for Space Transport Systems research project, funded by the Italian Space Agency.

Nomenclature

A	=	source strength
c	=	speed of sound
D	=	jet diameter
$\mathcal{D}$	=	directivity factor
F	=	rocket thrust
$\mathcal{F}$	=	dimensionless function
f	=	acoustic frequency
G	=	Green's function
G^I	=	least-squares pseudoinverse matrix
H	=	Heaviside function
h	=	launcher altitude with respect to the pallet
I	=	acoustic intensity
i	=	imaginary unit, $i = (\sqrt{-1})$
k	=	acoustic wave number, $k = \omega/c_a$
L_c	=	jet laminar core length
L_{ref}	=	jet reference length
L_s	=	jet supersonic cone length
L_{xyz}	=	computational aeroacoustics grid box dimensions
M	=	Mach number
M_r	=	Mach vector projection along the source to observer direction, $M_r = \mathbf{M} \cdot (\mathbf{x} - \mathbf{x}_n)$
$\mathbf{n}$	=	unit normal vector
p	=	pressure
p_{ref}	=	reference sound pressure level, 2×10^{-5} Pa
Re	=	Reynolds number
r, θ	=	spherical coordinates
St	=	Strouhal number (reduced frequency)
s	=	jet line curvilinear abscissa
T	=	temperature
W_{ac}	=	acoustic power
$\mathbf{U}$	=	mean flow velocity
$\mathbf{u}$	=	velocity
W_m	=	mechanical power
W_{ref}	=	reference sound power level, 1×10^{-12} W
$\tilde{w}, \tilde{\tilde{w}}$	=	reduced sound power spectral densities
w	=	power spectral density
α	=	wave number in the streamwise direction
β	=	Prandtl–Glauert factor, $\beta^2 = 1 - M^2$
γ	=	ratio of specific heats of the gas
η	=	acoustic efficiency of the jet
Θ	=	Mach cone factor, $\Theta = M_r^2 + \beta^2$
λ	=	sound wavelength
ρ	=	density
σ	=	relative sound power along the jet center line
ϕ	=	velocity potential, $\mathbf{u} = \nabla\phi$
ω	=	radian frequency

Subscripts

0	=	mean flow quantities
a	=	atmospheric ambient quantities
e	=	nozzle exhaust quantities
j	=	fully expanded jet quantities

Presented as Paper 2939 at the 14th AIAA/CEAS Aeroacoustics Conference (29th AIAA Aeroacoustics Conference), Vancouver British Columbia, 5–7 May 2008; received 19 May 2008; accepted for publication 24 February 2009.

*Senior Research Engineer, Rotorcraft Aerodynamics and Aeroacoustics Laboratory. Member AIAA.
†Junior Research Engineer, Rotorcraft Aerodynamics and Aeroacoustics Laboratory.
‡Responsible for Aerothermodynamics, Mechanical Subsystem Group.
§Product Engineer, Mechanical Design Group, Space Division.

m = Green's function discretization stencil node index
n = Green's function discretization shape function index
t = nozzle throat quantities

Superscripts

$'$ = perturbation quantities
$\check{}$ = Fourier component in frequency/axial wave number space
$\hat{}$ = Fourier component in frequency space
$\bar{}$ = time average
$\tilde{}$ = dimensionless mean flow quantities and sound spectral densities

I. Introduction

THE hot supersonic turbulent jet plume from the rocket exhaust of a launch vehicle generates a severe acoustic environment that induces strong vibrations on the structural components of the launcher and its payload. The numerical prediction of the vibroacoustic response during liftoff conditions requires as an input an accurate knowledge of the environmental sound power spectrum, directivity, and spatial correlation. Computational fluid dynamics (CFD)/computational aeroacoustics (CAA) methods that are typically used for jet noise predictions in aeronautical applications cannot be applied to a launch vehicle. On the one hand, hybrid methods based on unsteady CFD simulations of the turbulent jet stream and its interaction with the launch pad matched with acoustic analogy formulations, both integral [1,2] or differential [3–6], are still too cumbersome for rocket noise applications. On the other hand, semi-empirical methods based on acoustic analogy formulations applied to statistical representations of the turbulent flowfield [7–9], although satisfactory for the prediction of small-scale turbulent mixing noise at 90 deg from the jet direction, are lacking in many phenomenological aspects, such as those related to mean flow temperature gradients and temperature fluctuations in very hot jets, the turbulence/shock interaction in imperfectly expanded jets, and noise reflections from the launch pad.

In this scenario, empirical methods based on simple heuristic assumptions and scaling laws, properly tuned against experimental data from different rocket engines, still provide a viable solution for the preliminary design of a launch vehicle. The most popular empirical model was developed by Eldred at NASA [10] during the 1970s and successively modified by several authors [11–15], mainly in France during the qualification of the Ariane 1 and 5 space launchers. In the present paper, we use two different formulations of Eldred's rocket noise model to reproduce the acoustic environment of the launch vehicle Vega.

Vega is the European small launch vehicle under development by the prime contractor European Launch Vehicle S.p.A. (ELV) in the frame of an ESA contract. It is constituted of four stages, and it is targeted to the scientific/commercial market of small satellites (300–2500 kg) into low Earth orbits, with inclinations ranging from 5.2 deg up to sun-synchronous orbits and with altitudes ranging from 300 to 1500 km. The first-stage motor is the P80, a carbon-epoxy filament-wound monolithic motor case produced by EUROPROPULSION, an Avio/Société Nationale d'Étude et de Construction de Moteurs d'Aviation joint venture. Vega has successfully completed the system-critical design review, and most of its motors and structures are already qualified. The qualification flight is scheduled for 2009 from the refurbished ELA-1 launch pad (now Vega pad) of the European Space Center in French Guiana. The availability of noise measurements were carried out during the Vega development phase by Avio and the Office National d'Études et de Recherches Aérospatiales (ONERA) [16,17] using a $1/20$ scaled mock-up in the Avio facility Banco Esperimenti Acustici (Acoustic Test Bench) located in Colleferro and the scheduled new tests to be performed in the framework of the Italian Space Agency funded project CAST give us the opportunity to improve the existing empirical methods by means of more sophisticated CFD/CAA methods.

As a first step, we compare the results obtained by employing two variants of Eldred's model in connection with Varnier's core length correction [12] against the available experimental data. Standard jet quantities are used, and no attempt to tune the empirical prediction is made. In a second step, which represents the original contribution of this paper, we use a frequency-domain CAA method to propagate the noise generated by a certain number of elementary sources distributed along the jet plume. Uncorrelated superimpositions of these elementary fields, weighted by a source magnitude distribution coming from the same heuristic arguments employed in Eldred's model, provide an equivalent acoustic environment to be compared with the fully empirical prediction based on Eldred's model. Emphasis is placed on sound scattering effects due to the launcher and the pad and their possible role in explaining some discrepancies between the measured noise spectra and the fully empirical prediction.

The paper is organized as follows. In Sec. II, the empirical noise source model and the analytical propagation model through a semi-infinite space are presented. In Sec. III, the numerical method used to compute the noise field generated by elementary sources distributed along the jet plume is described, with a focus on the limits of validity of the employed physical model and on the automatic grid generation approach. In Sec. IV, details about the overall launch configuration and the operating conditions used for the validation of the noise prediction are described. Results for both the empirical and hybrid empirical/CAA methods are presented in Sec. V. Finally, the main achievements of the present study are summarized in Sec. VI, together with an outlook on future activities.

II. Empirical Jet Source and Propagation Model

Following the dimensional analysis carried out by many authors (see, for instance, [11,15]), the mean square acoustic pressure in a spherical reference system of coordinates r and θ can be expressed as

$$\bar{p'^2}(r,\theta) = \rho_j^2 U_j^4 (D_j^2/r_j^2)\mathcal{F}_1[\theta, (p_j/p_a), (\rho_j/\rho_a), (c_j/c_a), M_j, Re_j] \quad (1)$$

The corresponding far-field intensity can be written as

$$I(r,\theta) = \bar{p'^2}/(\rho_a c_a) = \rho_j U_j^3 (D_j^2/r_j^2)\mathcal{F}_2[\theta, (p_j/p_a), (\rho_j/\rho_a), (c_j/c_a), M_j, Re_j] \quad (2)$$

Hence, integrating over a sphere of radius r, the overall sound power takes the following form:

$$W_{\mathrm{ac}} = \rho_j U_j^3 D_j^2 \mathcal{F}_3[(p_j/p_a), (\rho_j/\rho_a), (c_j/c_a), M_j, Re_j] \quad (3)$$

Throughout the paper, the functions $\mathcal{F}_i$ depend only on dimensionless quantities. Equation (3) is in agreement with the M_j^3 power law obtained by Ffowcs-Williams [18] for the noise generated by the supersonic convection of turbulent eddies, the so-called Mach wave radiation phenomenon. Moreover, the group $\rho_j U_j^3 D_j^2$ is proportional to the mechanical power W_m developed by the jet flow. Thus, Eq. (3) can be written as

$$W_{\mathrm{ac}} = W_m \eta[(p_j/p_a), (\rho_j/\rho_a), (c_j/c_a), M_j, Re_j] \quad (4)$$

where the dimensionless quantity η plays the role of an acoustic efficiency of the jet. This acoustic efficiency has been determined experimentally by Eldred for a great number and variety of rockets and for different exhaust conditions. The measurements state that η is a weak function of its arguments and, for practical applications, it can be assumed to be constant. Typical values for undeflected jets are in the interval [0.1%, 1%], with clustering in the interval [0.2%, 0.5%]. An empirical law proposed by Sutherland [19] reads

$$\eta = 0.0012(\gamma_j/\gamma_a)(c_t/c_a)^3(c_t/U_e)^2 \quad (5)$$

and provides values of η around 0.53%. This is the value used to obtain the results presented in Sec. V.

Because of the random nature of the aeroacoustic mechanisms involved in the jet noise generation, the overall acoustic energy W_{ac} is distributed on a broad band spectrum. Therefore, introducing the reduced frequency $St = fD_j/U_j$ and performing the same dimensional analysis as before, the power spectral density can be written as

$$w(St) = \rho_j U_j^3 D_j^2 (D_j/U_j)\mathcal{F}_4[\mathrm{St}, (p_j/p_a), (\rho_j/\rho_a), (c_j/c_a), M_j, Re_j] \tag{6}$$

From Eqs. (3) and (6), it results that

$$\tilde{w}(St) \equiv \frac{w(St)}{W_{ac}}\frac{U_j}{D_j} = \frac{\mathcal{F}_4}{\mathcal{F}_3} \equiv \mathcal{F}_5(St) \tag{7}$$

where the reduced power spectral density $\tilde{w}$ has been introduced, so that

$$\int_0^\infty \tilde{w}(St)\,\mathrm{d}St = 1$$

The regression law (7) has been confirmed by Eldred by collecting noise measurements for a large number of different rockets, as shown in Fig. 1.

Finally, by supposing that the acoustic energy distributed in the ith discrete frequency is concentrated into an equivalent monopole of strength A_i, it results that

$$A_i = \sqrt{(\rho_a c_a/2\pi)\eta W_m (D_j/U_j)\Delta f_i \tilde{w}(St)} \tag{8}$$

The next step consists of localizing the sources in the jet plume and computing the overall sound pressure level at an observation point in the far field.

The first method, proposed by Eldred and employed by Candel [11] to estimate the acoustic levels around the Ariane I launch vehicle, is based on the observation that each slice of the jet contributes to the acoustic radiation, mostly in a frequency band f_i that depends on the distance of the slice from the exhaust. Indeed, because the size of the turbulent structures increases as their distance from the exhaust increases, the acoustic peak frequency band for each slice is a decreasing function of the slice distance from the exhaust. The curvilinear distance s_i, as sketched in Fig. 2, of a jet slice that emits in the frequency band f_i can be determined through the empirical curves plotted in Fig. 3. The prediction of the far-field acoustic spectra is thus performed by looping over the frequency bands of interest and, for each frequency, the jet-local spherical coordinates (r_i^+, θ_i^+) and (r_i^-, θ_i^-) corresponding to the ith jet slice and its ground-reflected image are determined, respectively, as sketched in Fig. 2.

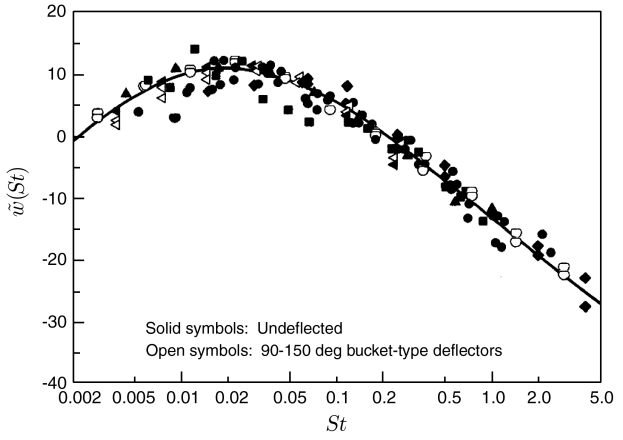

Fig. 1 Reduced power spectral density as a function of the reduced frequency *St*. Adapted from [10].

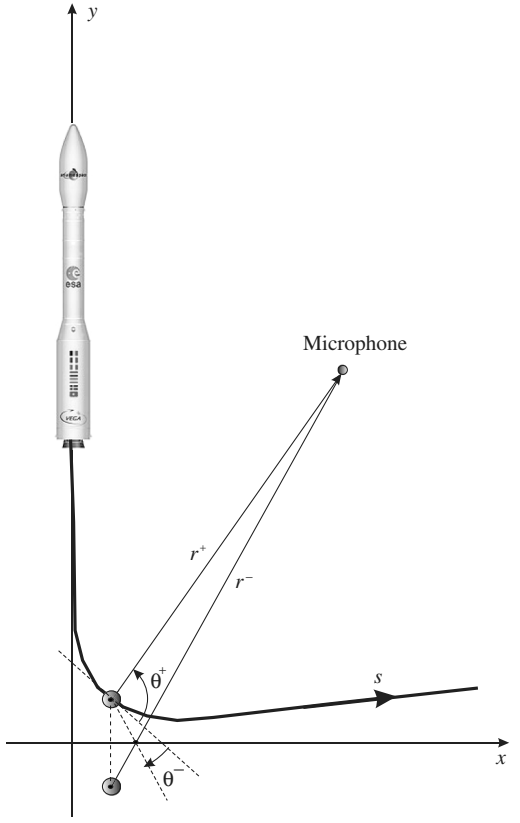

Fig. 2 Equivalent source distribution along the jet plume and coordinate system representation.

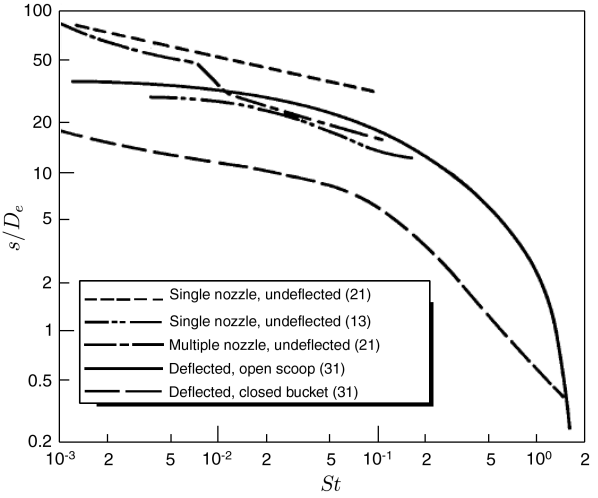

Fig. 3 Source curvilinear distance from the jet exhaust as a function of the reduced frequency *St* for different chemical rockets. Adapted from [10].

Translating Eq. (7) into sound power levels (PWL) yields

$$\mathrm{PWL}_i = 10\log[\tilde{w}(St_i)] + 10\log(W_{ac}/W_{ref}) + 10\log(\Delta f_i) - 10\log(U_j/D_j) \tag{9}$$

where W_{ref} denotes the reference sound power level. The mean square pressure generated by an equivalent elementary source corresponding to the ith jet slice can be written as

$$\bar{p'^2}_i(r_i, \theta_i, \mathrm{St}_i) = (A_i^2/2r_i^2)\mathcal{D}_i(\theta_i, St_i) \tag{10}$$

where $\mathcal{D}_i(\theta, St)$ is a dimensionless directivity function accounting for the mean flow refraction effects for the ith noise frequency

component. Making use of Eqs. (8) and (10), the sound pressure level (SPL) generated by the ith jet slice can be written as

$$\mathrm{SPL}_i = \mathrm{PWL}_i - 10\log(r_i^2) + 10\log(\mathcal{D}_i(\theta_i, St_i)) - 10\log\left(\frac{p_{\mathrm{ref}}^2 4\pi}{W_{\mathrm{ref}}\rho_a c_a}\right) \tag{11}$$

where p_{ref} denotes the reference sound pressure level. The directivity sound level factor $10\log(\mathcal{D}_i)$ can be determined by the curves plotted in Fig. 4. Finally, the overall sound pressure level (OASPL) is computed by assuming fully uncorrelated elementary source fields and performing a logarithmic summation over all the jet slices and their images, that is,

$$\mathrm{OASPL} = 10\log\left(\sum_{i+} 10^{\mathrm{SPL}_{i+}/10} + \sum_{i-} 10^{\mathrm{SPL}_{i-}/10}\right) \tag{12}$$

The second method, proposed by Eldred and successively modified by Varnier [12] by observations carried out on several scaled rocket models, is based on the observation that each jet slice contributes to the full noise spectral frequency content with an overall power level that depends on its curvilinear distance from the exhaust. Hence, denoting with subscript k the kth slice at a distance s_k from the exhaust, the corresponding acoustic power can be written as

$$w(s_k)\Delta s_k \equiv \frac{L_{\mathrm{ref}} w(s_k)}{W_{\mathrm{ac}}} W_{\mathrm{ac}} \frac{\Delta s_k}{L_{\mathrm{ref}}} \tag{13}$$

where $w(s_k)$ denotes a sound power per unit axial length, and L_{ref} is a jet reference length. In high-speed turbulent jets, the noise is mainly generated in the supersonic cone and the acoustic levels are proportional to the amount of turbulent kinetic energy. Therefore, the normalized acoustic power level

$$\sigma\left(\frac{s}{L_{\mathrm{ref}}}\right) = \frac{L_{\mathrm{ref}} w(s_k)}{W_{\mathrm{ac}}} \tag{14}$$

increases along the jet line, reaching its maximum value close to the end of the supersonic cone. The empirical law employed by Eldred is plotted in Fig. 5. It shows that the acoustic power peaks at a distance of about $1.5L_{\mathrm{ref}}$ from the exhaust and that the jet is acoustically effective up to a distance of about $5L_{\mathrm{ref}}$, provided that L_{ref} denotes the laminar core length for which he provided the empirical formula $L_c = 3.45D_e(1 + 0.38M_j)^2$. Indeed, this is an unclear point of Eldred's empirical approach, as also argued by Varnier [12]. Varnier provided some experimental evidence for the sound power peaking at a distance between the end of the laminar core, L_c, and the end of the supersonic cone, L_s. However, he failed to establish a clear relationship between the reference length and these physically meaningful quantities and used the relationship

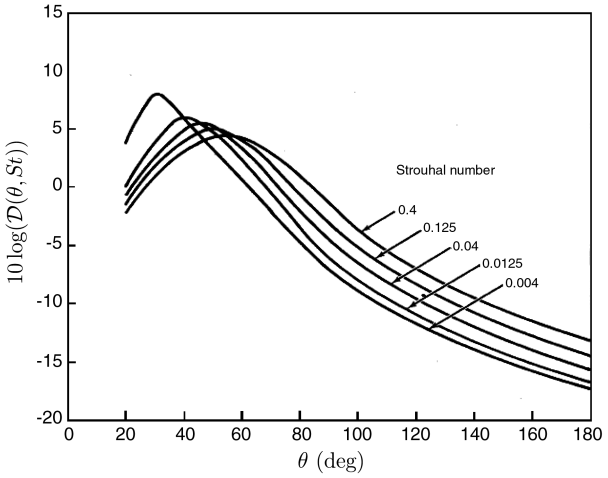

Fig. 4 Directivity sound level factor as a function of the observation angle θ and reduced frequency St. Adapted from [10].

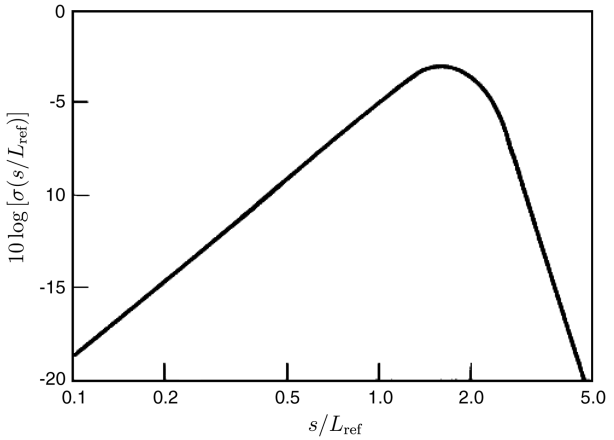

Fig. 5 Relative sound power distribution along the jet centerline for standard chemical rockets. Adapted from [10].

$$L_{\mathrm{ref}} = 1.75D_j(1 + 0.38M_j)^2 \tag{15}$$

which provides smaller values of the reference length than the previous one proposed by Eldred. The key point of Varnier's modification of Eldred's model is, therefore, to use the fully expanded Mach number

$$M_j = \left\{\frac{2}{\gamma_j - 1}\left[\left(1 + \frac{\gamma_j - 1}{2}M_e^2\right)\left(\frac{p_e}{p_a}\right)^{\frac{\gamma_j - 1}{\gamma_j}} - 1\right]\right\}^{1/2} \tag{16}$$

and the fully expanded jet diameter

$$D_j = \frac{2}{M_j}\sqrt{\frac{F}{\pi p_a \gamma_j}} \tag{17}$$

instead of the exhaust data in the determination of the reference length.

The overall power density level, $w(s_k)$, can be distributed on the frequency spectrum. Thus, denoting as $w(s_k, f_i)$ the sound power level per unit axial length and frequency and introducing the reduced sound power density

$$\tilde{\tilde{w}}(s_k, St_i) = \frac{w(s_k, f_i)}{w(s_k)}\frac{U_j}{s_k}\frac{c_a}{c_j} \tag{18}$$

the sound power level in the ith frequency band generated by the kth slice can be written as

$$\begin{aligned}\mathrm{PWL}_{ik} &\equiv 10\log(w(s_k, f_i)\Delta s_k \Delta f_i) \\ &= 10\log(\tilde{\tilde{w}}(s_k, St_i)) + 10\log(\sigma_k) + 10\log(W_{\mathrm{ac}}/W_{\mathrm{ref}}) \\ &\quad + 10\log\left(\frac{\Delta s_k}{L_{\mathrm{ref}}}\right) - 10\log\left(\frac{U_j c_a}{s_k c_j}\right) + 10\log(\Delta f_i)\end{aligned} \tag{19}$$

By performing a regression analysis of noise data from different chemical rockets, Eldred observed that the reduced sound power density $\tilde{\tilde{w}}(s_k, St_i)$ is a function of the modified reduced frequency St_i (s_k/D_j) (c_j/c_a). Hence, the reduced sound power density $\tilde{\tilde{w}}$ can be determined through the empirical curves plotted in Fig. 6. Analogous to Eq. (11), the sound pressure level corresponding to the ith frequency band and kth jet slice takes the form

$$\mathrm{SPL}_{ik} = \mathrm{PWL}_{ik} - 10\log(r_i^2) + 10\log(\mathcal{D}_i(\theta_i, St_i)) - 10\log\left(\frac{p_{\mathrm{ref}}^2 4\pi}{W_{\mathrm{ref}}\rho_a c_a}\right) \tag{20}$$

and the overall sound pressure level is obtained by double logarithmic summation over all the frequency bands and jet plume slices and their images. Finally, by supposing that the acoustic energy distributed in the ith discrete frequency and radiated from a jet slice of length Δs_k is concentrated into an equivalent source of strength, A_{ik}, it results that

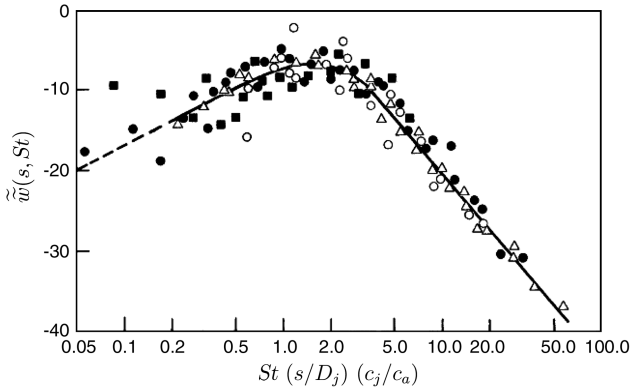

Fig. 6 Reduced sound power density as a function of the modified reduced frequency. Adapted from [10].

$$A_{ik} = \sqrt{\frac{\rho_a c_a}{2\pi}\eta W_m \tilde{\tilde{w}}(s_k, St_i)\sigma(s_k/L_{\text{ref}})\frac{s_k c_j}{L_{\text{ref}} U_j c_a}\Delta s_k \Delta f_i} \quad (21)$$

III. Computational Aeroacoustics Propagation Model

The original contribution of this work consists of improving the empirical rocket noise model described in Sec. II by replacing the analytical and empirical propagation factors $-10\log(r^2)+10\log(\mathcal{D}(\theta, \text{St}))$ in Eq. (20) with a CAA code employing a Green's function discretization (GFD) [20–22]. The uncorrelated source strength distribution (21) is then used to convolute a precomputed set of elementary source fields. The CAA prediction is carried out by solving, for each elementary source along the jet stream, a convected wave equation within a computational domain for which the far-field extension decreases as the frequency increases. This approach allows for the control of the number of degrees of freedom at each frequency. A Cartesian grid is generated automatically for each frequency and used in connection with an immersed-boundary approach [23]. The mean flow for realistic operating conditions has been computed by means of the commercial CFD software FLUENT and a body-conforming unstructured grid.

A. Governing Equations

The wave model used in this work is derived from the convected wave equation for the acoustic velocity potential ϕ and a generic rotational mean flow discussed by Pierce [24]. Even though this model is rigorously valid only for mean flows that vary slowly over the length and time scales of the sound waves (high-frequency approximation), it constitutes a convenient alternative to the linearized Euler equations in some practical applications. Starting from the time-domain wave equation

$$(1/\rho_0)\nabla\cdot(\rho_0\nabla\phi) - D_t(D_t\phi/c_0^2) = 0 \quad (22)$$

with $D_t = \partial/\partial t + \mathbf{U}_0\cdot\nabla$ denoting the convective time derivative, and making use of the dimensionless mean flow density $\tilde{\rho} = \rho_0/\rho_a$, temperature $\tilde{T} = T_0/T_a$, and velocity $\tilde{\mathbf{U}} = \mathbf{U}_0/c_a$, the following frequency-domain convected wave equation ($-i\omega t$ convention) can be obtained:

$$(\nabla\tilde{\rho}/\tilde{\rho})\cdot\nabla\hat{\phi} + \nabla^2\hat{\phi} - \frac{1}{\tilde{T}}(-ik + \tilde{\mathbf{U}}\cdot\nabla)^2\hat{\phi} + [(\tilde{\mathbf{U}}\cdot\nabla\tilde{T})/\tilde{T}^2](-ik + \tilde{\mathbf{U}}\cdot\nabla)\hat{\phi} = 0 \quad (23)$$

where $k = \omega/c_a$ is the acoustic wave number.

The applicability of such a simplified wave model to the complex jet stream of a rocket is reasonably questionable. Indeed, due to the presence of shocks and shear layers, the high-frequency limit is not reached by all the noise spectral components. Because it is very difficult or even impossible to determine a relationship between the modeling error and the frequency of the acoustic field for a realistic case, we can discuss the applicability of Pierce's wave model in the frequency range of interest by making three further simplifications. The first consists of assuming freejet conditions and neglecting any interaction effects with the launch pad. The second consists of supposing that the nozzle conditions are perfectly adapted to the ambient conditions, thus assuming fully expanded conditions to model the jet plume. The third consists of neglecting the axial mean flow gradients and supposing that the pressure perturbation field can be modeled by a Pridmore-Brown [25] third-order wave operator in the form used by Lilley to model the acoustic field in a parallel shear jet [26].

Let us consider the following third-order wave equation for the time Fourier component of the pressure perturbation:

$$\left[\hat{D}^3 - c_0^2\left(\hat{D}\nabla^2 - \frac{1}{\rho_0}\frac{\mathrm{d}\rho_0}{\mathrm{d}y}\hat{D}\frac{\partial}{\partial y} - 2\frac{\mathrm{d}U_x}{\mathrm{d}y}\frac{\partial^2}{\partial x\partial y}\right)\right]\hat{p} = 0 \quad (24)$$

where $\hat{D} = -i\omega + U_x\partial/\partial x$ is the Fourier-transformed convective derivative operator. Considering harmonic components of wave number α in the axial direction, Eq. (24) can be reduced to a second-order wave equation:

$$\check{p}_{yy} + \left(\frac{\mathrm{d}U_x}{\mathrm{d}y}\frac{2\alpha}{\omega-\alpha U_x} - \frac{1}{\rho_0}\frac{\mathrm{d}\rho_0}{\mathrm{d}y}\right)\check{p}_y + \left[\frac{(\omega-\alpha U_x)^2}{c_0^2} - \alpha^2\right]\check{p} = 0 \quad (25)$$

In the high-frequency limit, the axial harmonic component of the acoustic potential is the solution of the following second-order wave equation derived from Eq. (23):

$$\check{\phi}_{yy} + \frac{1}{\rho_0}\frac{\mathrm{d}\rho_0}{\mathrm{d}y}\check{\phi}_y + \left[\frac{(\omega-\alpha U_x)^2}{c_0^2} - \alpha^2\right]\check{\phi} = 0 \quad (26)$$

From the linearized pressure equation $\check{p} = i\rho_0(\omega-\alpha U_x)\check{\phi}$, the following relationships can be obtained:

$$\begin{aligned}
\check{\phi} &= -\frac{i}{\rho_0(\omega-\alpha U_x)}\check{p}\\
\check{\phi}_y &= -\frac{i}{\rho_0(\omega-\alpha U_x)}\check{p}_y + \frac{i}{\rho_0(\omega-\alpha U_x)}\left(\frac{1}{\rho_0}\frac{\mathrm{d}\rho_0}{\mathrm{d}y} - \frac{\alpha}{\omega-\alpha U_x}\frac{\mathrm{d}U_x}{\mathrm{d}y}\right)\check{p}\\
\check{\phi}_{yy} &= -\frac{i}{\rho_0(\omega-\alpha U_x)}\check{p}_{yy} + \frac{2i}{\rho_0(\omega-\alpha U_x)}\left(\frac{1}{\rho_0}\frac{\mathrm{d}\rho_0}{\mathrm{d}y} - \frac{\alpha}{\omega-\alpha U_x}\frac{\mathrm{d}U_x}{\mathrm{d}y}\right)\check{p}_y\\
&\quad + \left[\frac{\mathrm{d}}{\mathrm{d}y}\left(\frac{i}{\rho_0^2(\omega-\alpha U_x)}\frac{\mathrm{d}\rho_0}{\mathrm{d}y}\right) - i\alpha\frac{\mathrm{d}}{\mathrm{d}y}\left(\frac{1}{\rho_0(\omega-\alpha U_x)^2}\frac{\mathrm{d}U_x}{\mathrm{d}y}\right)\right]\check{p}
\end{aligned} \quad (27)$$

Hence, substituting the three quantities defined in Eq. (27) into Eq. (26) yields

$$\check{p}_{yy} + \left(\frac{\mathrm{d}U_x}{\mathrm{d}y}\frac{2\alpha}{\omega-\alpha U_x} - \frac{1}{\rho_0}\frac{\mathrm{d}\rho_0}{\mathrm{d}y}\right)\check{p}_y + \left[\frac{(\omega-\alpha U_x)^2}{c_0^2} - \alpha^2(1+\chi)\right]\check{p} = 0 \quad (28)$$

where

$$\begin{aligned}
\chi &= \frac{\rho_0(\omega-\alpha U_x)}{\alpha^2}\left[\frac{d}{dy}\left(\frac{1}{\alpha^2\rho_0^2(\omega-\alpha U_x)}\frac{d\rho_0}{dy}\right) - \alpha\frac{d}{dy}\left(\frac{1}{\rho_0(\omega-\alpha U_x)^2}\frac{dU_x}{dy}\right)\right]\\
&\quad + \frac{1}{\alpha^2\rho_0^2}\left(\frac{d\rho_0}{dy}\right)^2 - \frac{1}{\alpha\rho_0(\omega-\alpha U_x)}\frac{d\rho_0}{dy}\frac{dU_x}{dy}
\end{aligned} \quad (29)$$

Therefore, a comparison of Eqs. (25) and (28) reveals that, for values of $\chi \ll 1$, Pierce's wave model is consistent with the Lilley's wave model.

To estimate the value of the quantity χ for a jet at the same fully expanded conditions as the one from the Vega launcher during liftoff, the following empirical axial velocity field is assumed:

$$\frac{U_x}{M_j c_j} = \begin{cases} 1 & (x<L_c, y<d) \\ \exp[-\ell_n 2(y-d)^2/b^2] & (x<L_c, y\geq d) \\ \{1-\exp[0.5/(1-x/L_c)]\}\exp(-\ell_n 2y^2/b^2) & (x\geq L_c) \end{cases}$$

where $d = 0.5D_j(1 - x/L_c)$ and $b = D_j x/L_c$. The Crocco–Busemann formula is then used to compute the corresponding density field:

$$\rho_0 = \rho_j \left\{ \frac{T_a}{T_j} - \left(\frac{T_a}{T_j} - 1\right) \frac{U_x}{M_j c_j} + \frac{\gamma_j - 1}{2} \frac{M_j U_x}{c_j} \left(1 - \frac{U_x}{M_j c_j}\right) \right\}^{-1} \tag{30}$$

The mean flow contour levels are plotted in Fig. 7.

Equation (29) is computed at the axial location s of maximum source strength, which is extracted from the undeflected data plotted in Fig. 3, that is, $\log(s/D_j) = -0.2365\log(St) + 1.2405$. Furthermore, the larger streamwise acoustic wavelength is considered by setting $\alpha = k_0/(1 + M_x)$, $k_0 = \omega/c_0$ being the local acoustic wave number and $M_x = U_x/c_0$ the axial Mach number. The computation is carried out from band 14 (25 Hz) to 31 (1250 Hz), and the resulting values of χ are plotted in Fig. 8 against the frequency, the normalized axial distance s/D_j of maximum noise generation, the Strouhal number St, and the modified reduced frequency $St(s/D_j)(c_j/c_a)$. Both the maximum value of χ and its average value along the jet slice are plotted. These results can be used to establish a minimum frequency below which Pierce's wave model becomes unreliable. Setting arbitrarily to 0.1 the maximum acceptable value of χ, we can define the following conservative limits of applicability of the model: $f \gtrsim 120$ Hz, $St \gtrsim 0.1$, and $St(s/D_j)(c_j/c_a) \gtrsim 6$. These values correspond to the decreasing branch of the sound power spectral density at frequencies higher than the maximum sound power frequency, as shown in Figs. 1 and 6.

B. Discretization Scheme

Equation (23) is discretized by means of the unstructured finite difference scheme GFD. This is a wave-based scheme in which the expansion coefficients of an arbitrary derivative are obtained, for a generic computational stencil, by performing a least-squares inversion that projects the local reconstruction of $\hat{\phi}$ upon a combination of analytical solutions of the locally uniform convected Helmholtz equation. Finally, through analytical differentiation, shape functions for the arbitrary first- and second-order derivatives can be obtained and used to convert Eq. (23) into a linear system. The advantage of using the GFD scheme for the present CAA analysis is twofold. First, the scheme has spectral-like properties and preserves accuracy up to 3–4 grid points per acoustic wavelength [20,22,27]. And second, the same scheme can be easily used in connection with an immersed-boundary approach to discretize a slip boundary condition [23]. To describe this approach, some underlying elements about the GFD scheme are provided hereafter.

Consider a generic volume around the point **x** in which the acoustic potential $\hat{\phi}$ satisfies the convected Helmholtz equation, and

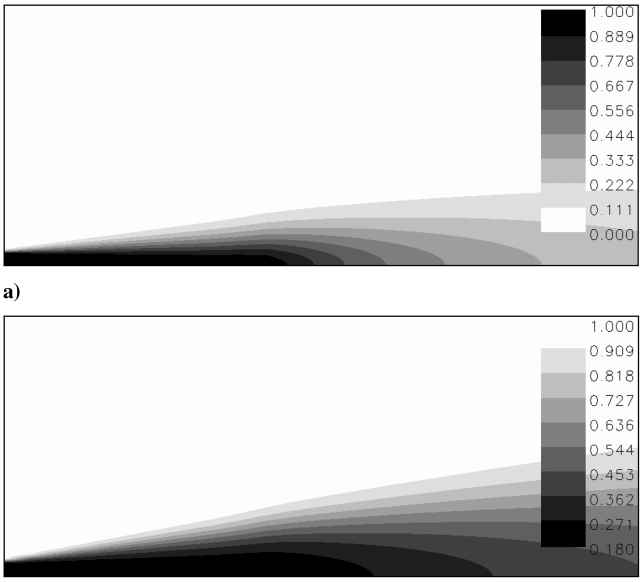

Fig. 7 Fully expanded jet plume: a) normalized axial velocity $U_x/(c_j M_j)$, and b) normalized density ρ_0/ρ_a.

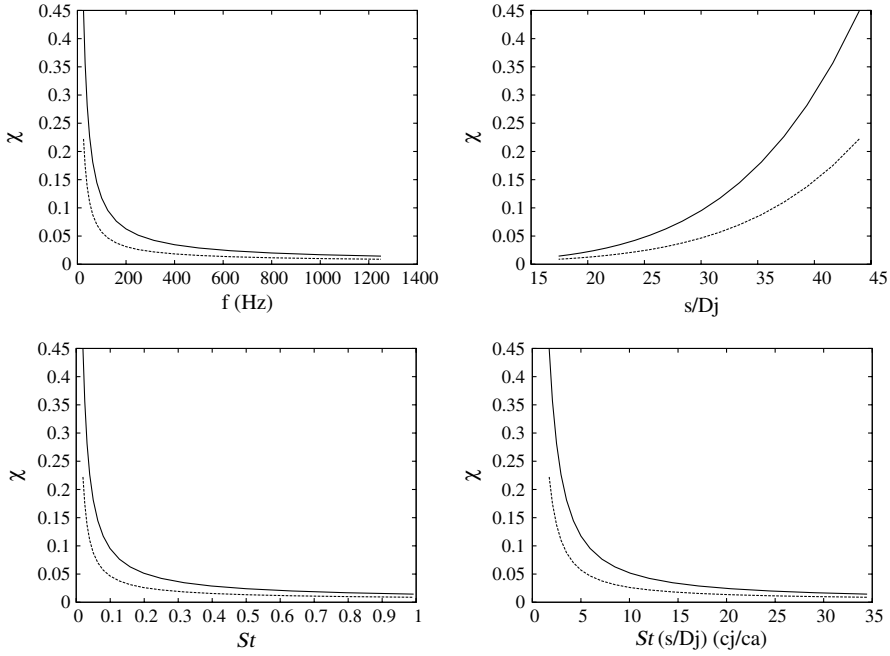

Fig. 8 Consistency analysis of Pierce's versus Lilley's wave equation for a fully expanded undeflected supersonic jet. Values of χ are computed along the axial slice s of maximum source strength and plotted against different quantities. Solid line: maximum values, dashed line: jet slice average values.

suppose that the values $\hat{\phi}_m = \hat{\phi}(\mathbf{x}_m)$ are prescribed at a certain number M of neighboring stencil points $\mathbf{x}_m$. By supposing that the acoustic field is locally generated by arbitrary distributions of N elementary sources at arbitrary locations $\mathbf{x}_n$, an interpolation formula can be derived from a compatibility condition between the acoustic potential at the M points and the convected Helmholtz equation, that is,

$$\hat{\phi}(\mathbf{x}) = \sum_{m=1}^{M} \sum_{n=1}^{N} G^I_{nm} G(\mathbf{x}, \mathbf{x}_n) \hat{\phi}_m \tag{31}$$

where

$$G(\mathbf{x}, \mathbf{x}_n) = \left\{ \frac{\exp[ikr(-M_r + \sqrt{\Theta}/\beta^2)]}{r\sqrt{\Theta}} + H(-\beta^2) \frac{\exp[ikr(-M_r - \sqrt{\Theta}/\beta^2)]}{r\sqrt{\Theta}} \right\} H(\Theta) \tag{32}$$

is Green's function of the convected Helmholtz equation for a subsonic and supersonic constant mean flow, and G^I_{nm} is the least-squares pseudoinverse of the influence matrix $G_{mn} \equiv G(\mathbf{x}_m, \mathbf{x}_n)$ $(N > M)$. Finally, by applying differential operators to Eq. (31), local approximations of the derivatives of $\phi(x)$ can be obtained and used to discretize Eq. (23) and all the boundary conditions.

C. Immersed-Boundary Approach

The immersed-boundary approach used for the present CAA analysis is based on three fundamental steps. The first step consists of using a ray-tracing algorithm to detect those cells of the CAA Cartesian grid that are cut by the surface mesh of the solid body and those cells that are completely encompassed by the body. The latter ones are removed from the computation. The second step consists of searching the intersections between the body surface elements and the grid segments connecting each inner node with the external ones (edges of the cut cells). Denoting as N the number of distinct intersections, a number of $N - 1$ new inner nodes are added to the original CAA mesh at the same location as the original inner node, as sketched in Fig. 9. Only one intersection point for each grid segment/surface element is permitted: the closest one to the inner node. Furthermore, additional nodes are not generated if two or more grid segments departing from the same inner node intersect two or more surface elements for which the relative angular deviation of the normal vectors does not exceed 45 deg. This condition guarantees that additional inner nodes are only generated close to the edges of the body. The new inner nodes are used to replace the original ones in the connectivity list of the corresponding cells, thus forcing a disconnection into the mesh. This allows the consideration of the effect of a thin septum on the scattered acoustic field, even when the septum contains only one layer of grid nodes, as sketched in Fig. 9. The third step consists of requiring that the potential at the M^i stencil nodes of each inner node i satisfies a compatibility condition with the slip condition at the corresponding intersection with the immersed surface. More precisely, considering the inner node $\mathbf{x}_i$ and its projection on the body $\mathbf{x}^\dagger_i$, Eq. (31) can be differentiated to write the following slip condition:

$$\sum_{m=1}^{M^i} \sum_{n=1}^{N} G^I_{nm} \hat{\phi}^i_m \nabla G(\mathbf{x}^\dagger_\mathbf{i}, \mathbf{x}_n) \cdot \mathbf{n}^\dagger = 0 \tag{33}$$

where $\mathbf{n}^\dagger$ denotes the unit normal vector at the projection point $\mathbf{x}^\dagger_i$.

In a previous work [23], the immersed-boundary formulation was verified by computing the sound transmission through a constant area duct and sound scattering from a sphere and by comparing the numerical solution with the analytical ones. The relative magnitude and phase L_2 errors not exceeding 2×10^{-3} were obtained by using about 10 grid nodes per acoustic wavelength. In the present work, the focus is on the modeling of the diffraction effects due to the presence of edges and thin septa in the scattering surface. Unfortunately, due to the lack of suitable benchmark problems, a rigorous verification is not possible. The alternative consists of using the numerical solution computed by a standard body-fitted approach as the reference solution. Because different meshes are employed for the immersed-boundary and body-fitted computations, the solutions are projected onto the same grid to be compared. Such a verification approach does not provide rigorous information about the accuracy of the method, because both the numerical solutions and their projections onto the common grid are affected by a discretization error. However, it does provide some evidence of the robustness of the method when applied to complex configurations.

The scattering of spherical waves by a rigid pyramid is the test case considered herein. This configuration allows the verification of the formulation in the presence of oblique edges. The dimensions are the same as the square-base Cheope's pyramid, with the base edge equal to 230.9 m and the height equal to 147 m. A monopole source of magnitude equal to 1×10^3 is located at the point $(-1 \times 10^3$ m, -1×10^3 m), the origin of the reference system being located at the center of the base. Two acoustic wavelengths are considered: $\lambda_1 = 34.6$ m and $\lambda_2 = 69.2$ m. The corresponding Cartesian grids are defined as -300 m $\le x, y \le 300$ m, $0 \le z \le 300$ m, and $\Delta = 5$ m for the first case and -600 m $\le x, y \le 600$ m, $0 \le z \le 600$ m, and $\Delta = 10$ m for the second case. Perfectly matched layer (PML) buffers with a thickness equal to 2λ are used to damp the outgoing scattered waves while setting the incident acoustic waves. The computational domain for the first case is shown in Fig. 10.

The reference body-fitted solutions have been computed by using unstructured tetrahedral meshes, generated by setting the mesh size

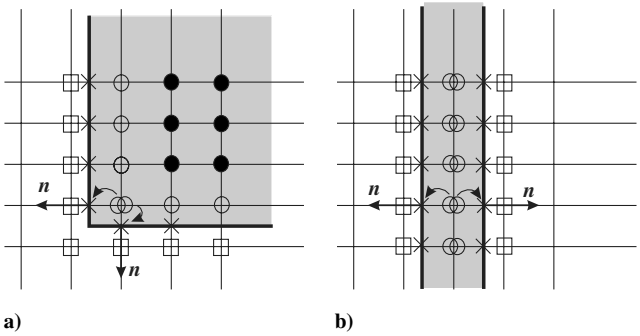

Fig. 9 Two-dimensional representation of the procedure employed to detect multiple intersections points between the cut cell edges (thin lines) and the immersed surface (thick lines): a) an example of an edge corner treatment, and b) an example of a thin septum treatment. Squares: outer nodes, open circles: inner nodes, closed circles: ineffective blanked nodes, ×: intersection nodes.

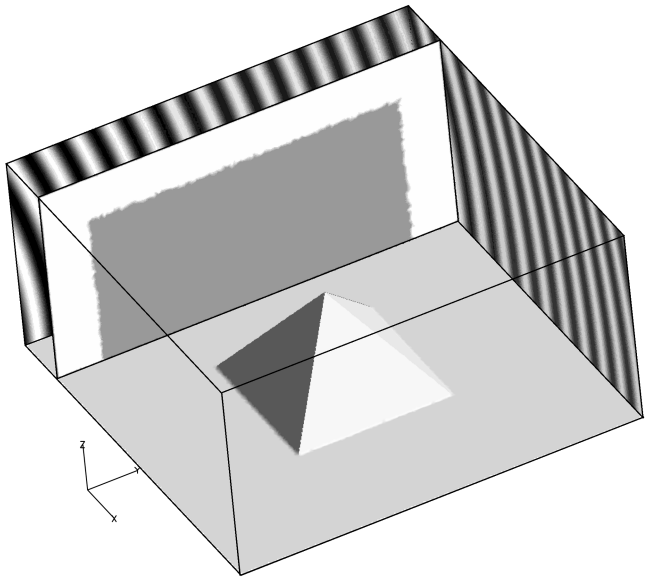

Fig. 10 Computational domain, PML buffers, and incident acoustic field for Cheope's pyramid scattering problem ($\lambda_1 = 34.6$ m).

on the boundary surfaces equal to 5 and 10 m, respectively. For the first case, the contour levels of the resulting minimum number of grid points per acoustic wavelength on the plane $y = 0$ are plotted in Fig. 11. A point-by-point comparison of the immersed-boundary and body-fitted results is then carried out by projecting the solutions onto three 2-D unstructured grids that lie on the planes $y = 0$ and $z = 72.5$ and 150 m.

The body-fitted and immersed-boundary results for the first case are shown in Figs. 12b and 12a, respectively. Contour levels are plotted for the real part of the acoustic potential projected on the plane $y = 0$. Some differences can be observed around the pyramid vertex, which is the most difficult geometrical detail to be featured by the immersed-boundary approach. Results on planes $z = 72.5$ and 150 m are shown in Fig. 13 for the same case. A good agreement can be observed on the plane $z = 72.5$ m, whereas some discrepancies in the wave diffraction pattern occur on the plane $z = 150$ m, which is immediately above the vertex of the pyramid.

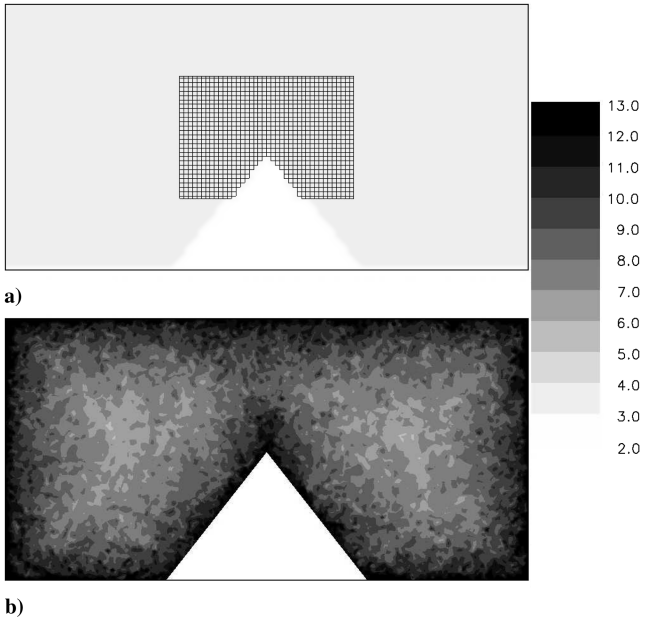

Fig. 11 Shown are the following: a) a subset of the Cartesian mesh ($\Delta = 5$ m), and b) the minimum number of grid points per acoustic wavelength on the plane $y = 0$ for an unstructured mesh of equivalent size.

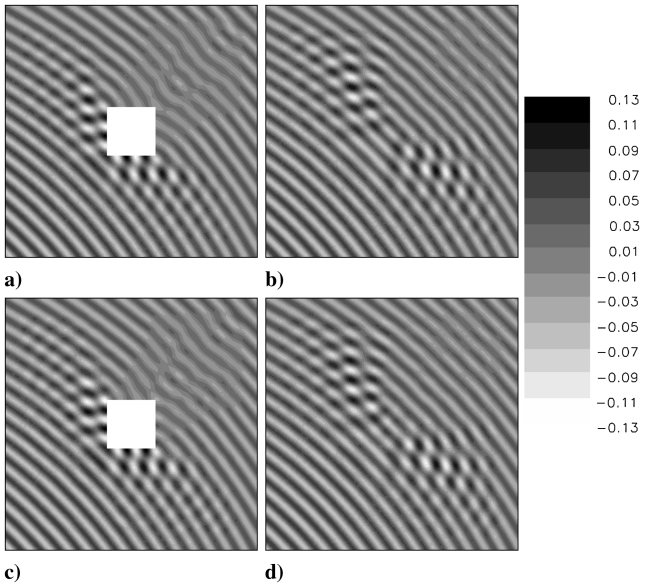

Fig. 13 Real part of the acoustic potential for the high-frequency case ($\lambda = 34.6$ m): a) body-fitted results on plane $z = 72.5$ m, b) body-fitted results on plane $z = 150$ m, c) immersed-boundary results on plane $z = 72.5$ m, and d) immersed-boundary results on plane $z = 150$ m.

Results for the second case are shown in Figs. 14 and 15. Because of the increased mesh size, the agreement between immersed-boundary and body-fitted results for this frequency is not as good as for the higher-frequency case: significant discrepancies take place in the diffraction pattern generated by the vertex of the pyramid.

A quantitative comparison is finally carried out by computing the relative magnitude and phase L_2 errors defined as

$$\mathrm{Err}_M = \sqrt{\frac{\sum_{i=1}^{\mathcal{N}} (|\phi^i| - |\phi_a^i|)^2}{\sum_{i=1}^{\mathcal{N}} |\phi_{\mathrm{ref}}^i|^2}}, \qquad \mathrm{Err}_\varphi = \sqrt{\frac{\sum_{i=1}^{\mathcal{N}} \min\{\varphi_1, \varphi_2\}}{4\pi^2 \mathcal{N}}} \tag{34}$$

where the subscript ref denotes the body-fitted solution, $\mathcal{N}$ is the number of points in the 2-D projection grid, $\varphi_1 = (\arg(\phi^i) -$

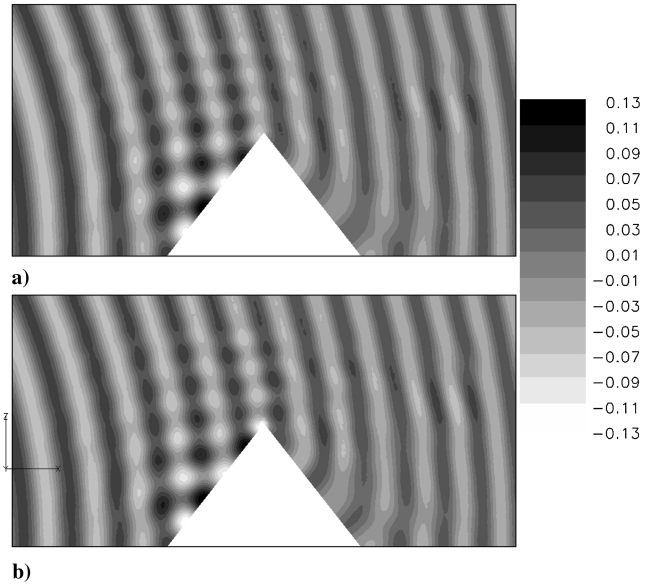

Fig. 12 Real part of the acoustic potential on the plane $y = 0$ for the high-frequency case ($\lambda = 34.6$ m): a) body-fitted results, and b) immersed-boundary results.

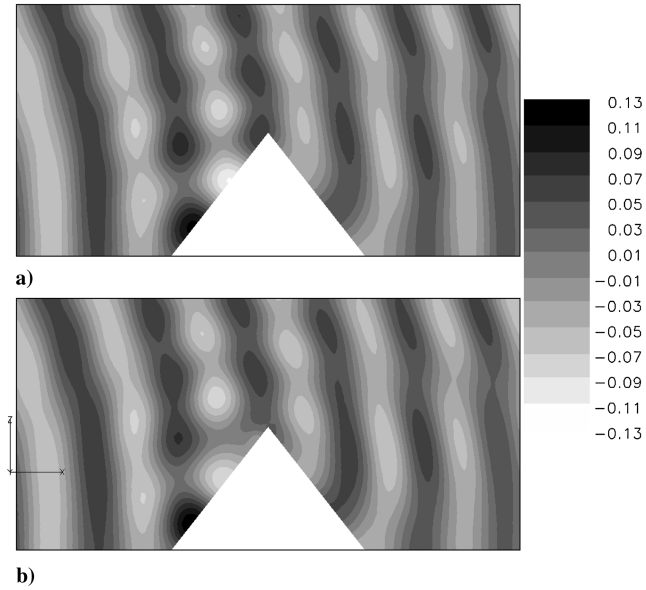

Fig. 14 Real part of the acoustic potential on the plane $y = 0$ for the low frequency case ($\lambda = 69.2$ m): a) body-fitted results, and b) immersed-boundary results.

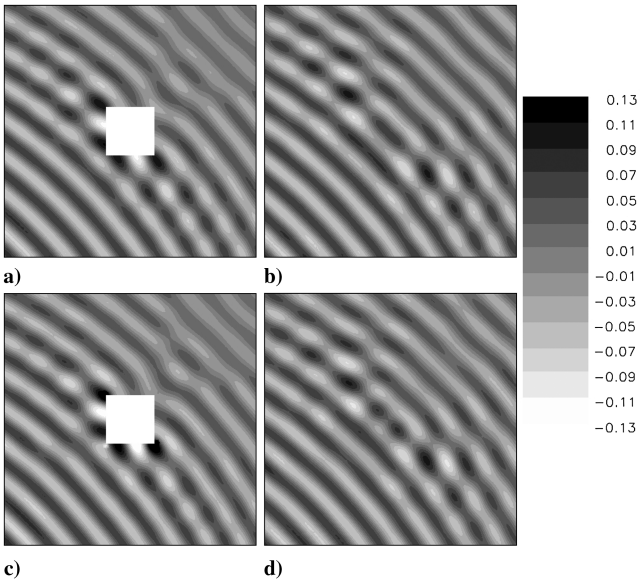

Fig. 15 Real part of the acoustic potential for the low-frequency case ($\lambda = 69.2$ m): a) body-fitted results on plane $z = 72.5$ m, b) body-fitted results on plane $z = 150$ m, c) immersed-boundary results on plane $z = 72.5$ m, and d) immersed-boundary results on plane $z = 150$ m.

$\arg(\phi^i_{\text{ref}}))^2$, and $\varphi_2 = (2\pi - |\arg(\phi^i) - \arg(p\phi^i_{\text{ref}})|)^2$. The computed values are reported in Table 1. The magnitude error exceeds 10% only for the low-frequency case on the plane $z = 72.5$ m, whereas the phase error does not exceed 2%. These values confirm the qualitative agreement previously observed and are herein provided as proof of the robustness of the immersed-boundary approach.

D. Multifrequency Grid Generation and Computational Setup

The frequency range covered by the present Vega launcher analysis is discretized in one-third octave bands, and computations are carried out from band 14 (25 Hz) to 30 (1000 Hz).

To contain the number of grid nodes at higher frequencies and, at the same time, to ensure a far-field boundary sufficiently far from the launcher, the size of the computational domain is varied with the acoustic wavelength λ_a according to the relationships $L_x = \max(8\lambda_a, 32\text{ m} + 5\lambda_a)$, $L_y = 46\text{ m} + 3\lambda_a + h$, and $L_z = \max(4\text{ m}, 6\lambda_a)$, with $h = 10$ m denoting the altitude of the launcher with respect to its steady location on the pallet. The resulting properties of the computational grids and the grid spacing Δ are shown in Table 2.

The coordinate system is shown in Fig. 16a, in which a shaded view of the Vega launcher and ELA-1 launch pad surfaces used for the automatic CAA grid generation are shown. The height of the Vega launcher is about 30 m; the basis of the deflector and its edge are about 15 and 10.5 m from the rocket exhaust, respectively. The Cartesian mesh is computed by requiring a constant spacing $\Delta = \min(\lambda_a/5, 0.68)$ in all directions, where $\lambda_a/5 = 0.68$ at a frequency of $f = 100$ Hz. This cutoff ratio permits the capture of important geometrical details of the launch system at low frequencies.

Table 1 Comparison between immersed-boundary and body-fitted results. Relative magnitude and phase L_2 errors (SI units)

Plane	λ	$\text{Err}_M \times 10^2$	$\text{Err}_\varphi \times 10^2$
$y = 0$	34.6	7.3	1.3
$z = 72.5$	34.6	7.8	1.9
$z = 150$	34.6	6.7	1.6
$y = 0$	69.2	9.8	1.9
$z = 72.5$	69.2	10.5	1.9
$z = 150$	69.2	7.8	1.6

A number of Dirac sources are distributed along the jet line. To easily treat the bifurcation of the jet stream on the deflector, two symmetric jet lines with respect to the plane $x = 0$ are considered, but separated by a distance equal to the nozzle radius, as sketched in Fig. 16b. Only one jet line is used in the numerical prediction, and the results for the symmetric one are obtained by symmetry during the postprocessing convolution phase. One-half of the overall mechanical power is attributed to this jet line. The source strengths at each discrete location along the jet line necessary for the convolution of the elementary source fields are provided by Eq. (21), derived from the second variant of Eldred's empirical model. The results reported in Sec. V have been obtained by using 30 elementary sources uniformly distributed from the launcher nozzle up to a distance of 16 m from the symmetry plane. At each frequency, the overall noise field is computed by supposing that the 60 sources distributed along the two symmetric jet lines are fully uncorrelated.

PML absorbing conditions [22,28] are used to avoid wave reflections at the far-field boundaries $x = \pm L_x/2$, $z = \pm L_z/2$, and $y = -16\text{ m} + L_y$. The PML buffer thickness is equal to $2\lambda_a$, and the PML damping constant is increased parabolically in the PML buffers from 0 to the maximum value of 2 at the boundaries.

IV. Case Study and Test Description

The Italian Aerospace Research Center (CIRA) and ELV, the latter being the prime contractor of the Vega program, are involved in the national research program CAST funded by the Italian Space Agency. The main objective of CAST is to improve, through the introduction of advanced chemical and radiation models into a CFD code for hypersonic flows, the aerothermodynamical predictive capabilities of a spacecraft in reentry conditions. A task of the project is devoted to the development of predictive capabilities for the liftoff aeroacoustics and blast-wave generation and propagation. In this task, an experimental campaign on the BEAT facility has been subcontracted by ELV to Avio and scheduled for the beginning of 2009. The fully empirical prediction described in the present work is part of the pretest activity, whereas the hybrid empirical/CAA prediction is part of the posttest activity for which source localization techniques and acoustic inversion models are developed by CIRA.

The pretest analysis has been carried out under the same conditions used in a previous experimental campaign carried out by Avio, ELV, and ONERA on the BEAT facility [16,17]. Both the Vega launcher and the ELA-1 launch pad were reproduced on a scale of 1/20. Their design was conceived to reproduce the same acoustic environment generated by the full-scale Vega first-stage solid rocket motor P80 at different launcher altitudes from 0 to 75 m (full-scale values), reproducing the first 4 s of the Vega launcher ascent trajectory at liftoff. The P80 simulator operates in the same pressure chamber and nozzle expansion ratio conditions of the full-scale

Table 2 Computational domain and CAA grid characteristic dimensions (SI units)

f	L_x	L_y	L_z	Δ	No. of nodes
25	110.76	97.53	83.07	0.68	729313
32	87.90	88.96	65.93	0.68	529425
40	75.26	81.96	51.92	0.68	418217
50	66.61	76.77	41.53	0.68	347252
63	59.47	72.48	32.96	0.68	293428
80	53.63	68.98	25.96	0.68	252749
100	49.31	66.38	20.77	0.68	224665
125	45.84	64.31	16.61	0.55	304201
160	42.82	62.49	12.98	0.43	450687
200	40.65	61.19	10.38	0.35	652879
250	38.92	60.15	8.31	0.28	957787
315	37.49	59.30	6.59	0.22	1440825
400	36.33	58.60	5.19	0.17	2220300
500	35.46	58.08	4.15	0.14	3351800
630	34.75	57.65	4.00	0.11	6237258
900	33.92	57.15	4.00	0.08	17434381
1000	33.73	57.04	4.00	0.07	23678929

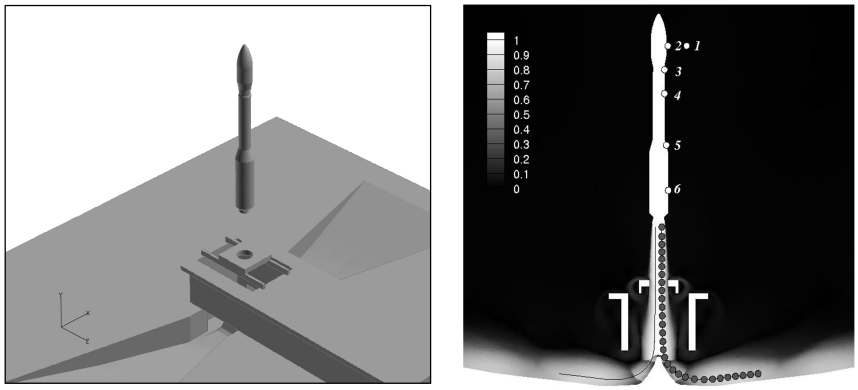

a) Reference system **b) Mean flow velocity magnitude normalized by the exhaust velocity**

Fig. 16 Vega launcher and ELA-1 launch pad configuration. In the right figure, the 30 Dirac sources and the symmetric ones used for the computation of the tailored Green's function are superimposed to the contour plots of the normalized mean flow velocity magnitude. In addition, the locations of the six microphones used throughout the paper are highlighted.

rocket motor; thus, it generates a jet plume that is characterized by the same Strouhal number, velocity, pressure, density, and temperature as the full-scale jet. Noise spectra in one-third octave bands have been measured at different axial and azimuthal locations along the launcher by means of flash-mounted, G.R.A.S. type 40BP microphones (which have a sensitivity of $\sim$1.4 mV/PA, a frequency range of 10 Hz–70 kHz, and a dynamic range of $<$174 dB). In addition, to quantify the noise diffraction effects due to the launcher, free-field noise spectra have been measured by means of G.R.A.S. type 40BE microphones (which have a sensitivity of $\sim$4 mV/PA, a frequency range of 4 Hz–100 kHz, and a dynamic range $<$166 dB) installed on a ring coaxial to the mock-up at the same axial and azimuthal locations of other flash-mounted microphones at the fairing level.

V. Numerical Results

A. Fully Empirical Prediction

Figure 17 compares the noise spectra measured by a microphone installed on the fairing of the launcher (microphone 2) and a microphone located at the same axial (y) and azimuthal (x/z) positions in the free-field (microphone 1) with the noise spectra computed by using the two variants of Eldred's empirical model. Results have been obtained by using an acoustic efficiency of 0.5%

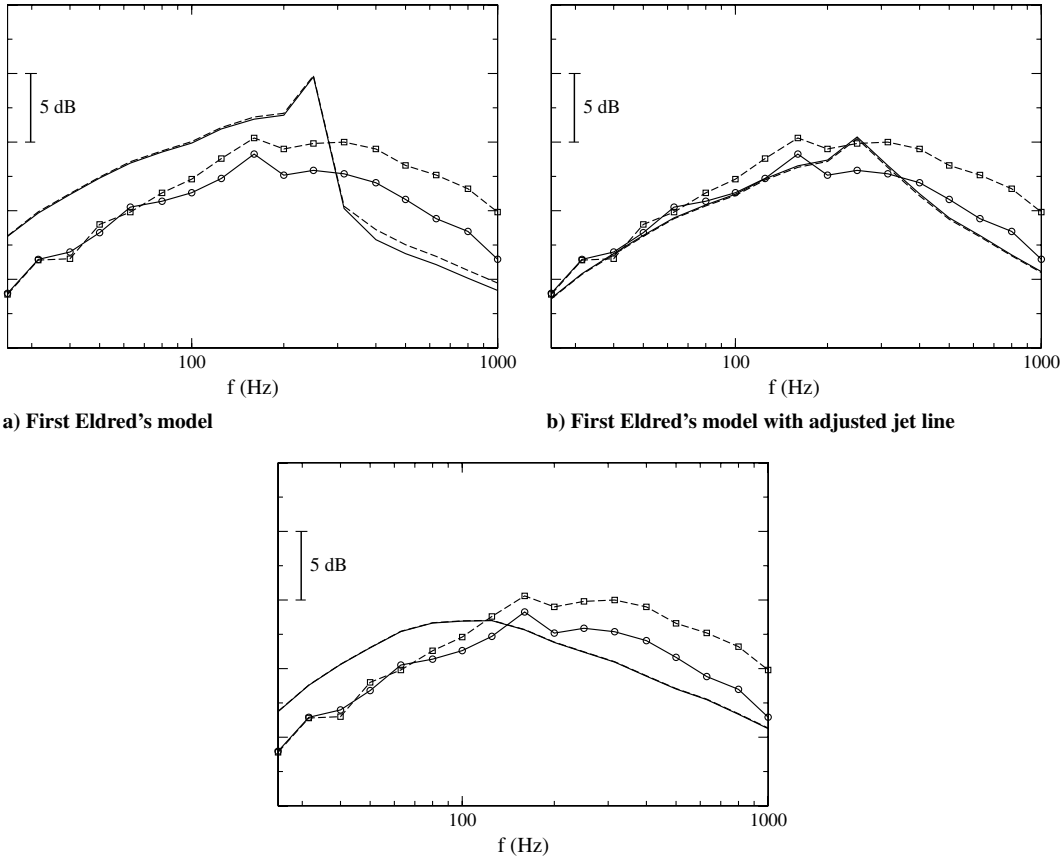

a) First Eldred's model **b) First Eldred's model with adjusted jet line**

c) Second Eldred's model

Fig. 17 Vega launcher one-third octave bands SPL. Comparison between experimental data (lines with symbols) and fully empirical predictions (lines). Microphone 1: solid lines and circles, microphone 2: dashed lines and squares.

and, for the second predictive model, by employing the reference length correction proposed by Varnier.

The results for the first model, plotted in Fig. 17a, predict fairly well the maximum noise frequency. The same noise levels are predicted for the fairing and free-field microphones, because the empirical model does not take into account the noise diffraction effects due to the launcher, and the distance between the two microphones is small compared with their distance from the jet sources. Conversely, the experimental data exhibit a significant difference between the fairing and free-field noise spectral levels that increases with the frequency from 0 up to about 3 dB. At lower frequencies, the noise levels are overestimated by 3–4 dB. At higher frequencies, the noise levels are underestimated by 2–3 dB on the fairing and by about 5 dB in the free field. The results are affected by an abrupt jump around 250 Hz, which is due to the simultaneous variation of the local radiation angle and frequency along the jet deflection, soon after the vertical segment of the jet line. This corresponds to an abrupt variation of the directivity factor extracted from the graph in Fig. 4. The main drawback of the first model, in fact, is that each jet slice is supposed to radiate noise in a narrow frequency band. Such a stiff behavior can be easily cured by introducing a small angular deflection into the vertical segment of the jet line. Results for an angular deflection of 10 deg are plotted in Fig. 17b. A significant improvement with respect to the previous results can be observed: the maximum noise frequency is predicted well without abrupt discontinuities, and the free-field noise levels are predicted with an accuracy of about 2 dB. Other model parameters could be varied to better fit the experimental results. However, such a tuning of the empirical model, although interesting for practical applications, is not in the scope of the present work. In fact, the main objective of this study is to build up the computational framework required by a source inverse model that will be used to generate input data for a vibroacoustical analysis.

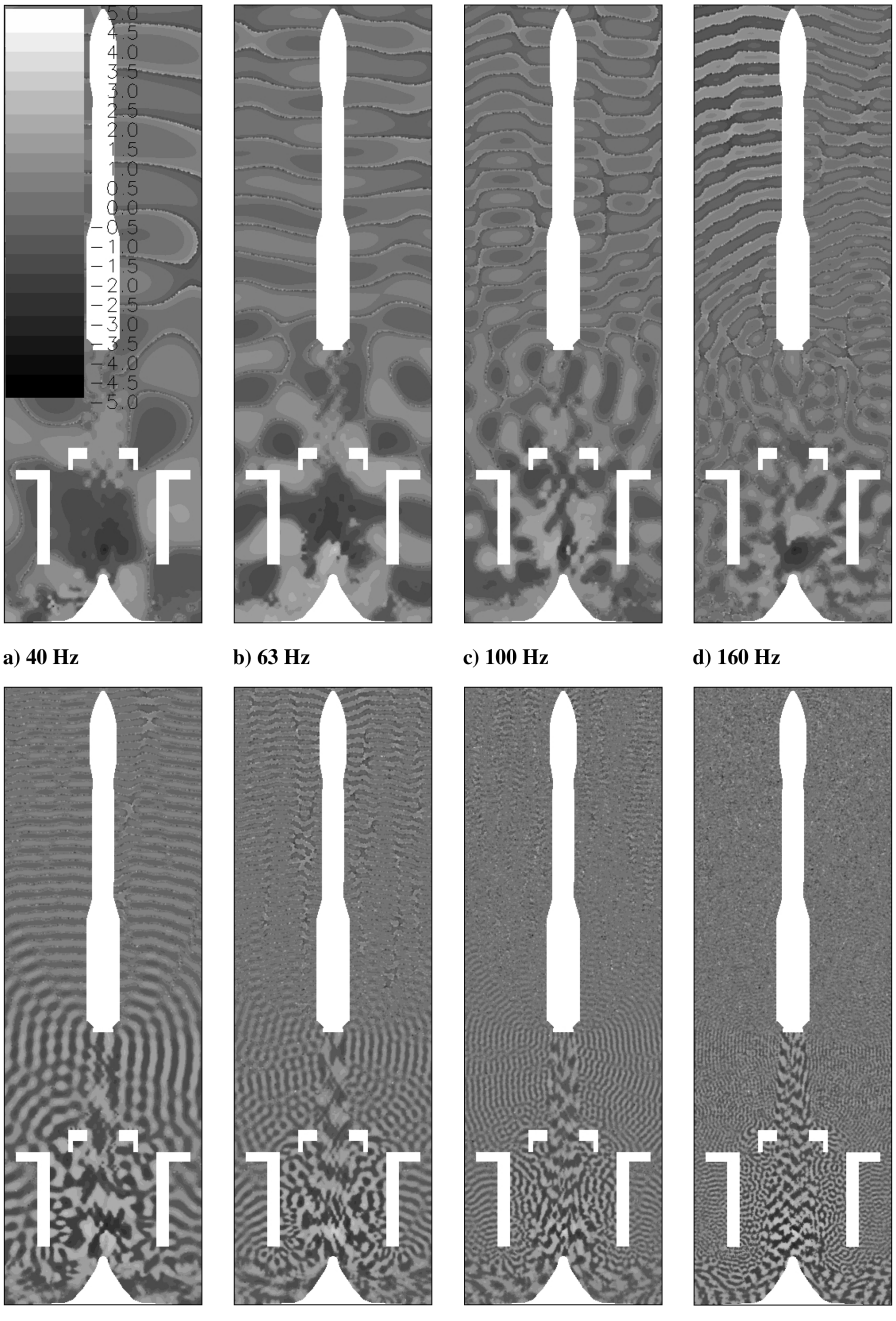

a) 40 Hz **b) 63 Hz** **c) 100 Hz** **d) 160 Hz**

e) 250 Hz **f) 400 Hz** **g) 630 Hz** **h) 1000 Hz**

Fig. 18 Normalized acoustic potential field $\log(|Re(\phi)|)\mathrm{sgn}(Re(\phi))$ generated by the fifteenth Dirac source in the rocket plume from the nozzle exhaust.

The results for the second model, plotted in Fig. 17c, exhibit a fairly better prediction of the spectral levels, with an accuracy between 3 and 5 dB all over the frequency range and about 2 dB for the overall sound power level. However, the maximum noise frequency is significantly underestimated. Again, because the noise diffraction effects are not taken into account by the model, the same noise levels are predicted at the fairing and free-field microphones, and the free-field prediction is slightly better than the fairing one. As pointed out for the first model, a tuning of the involved empirical quantities and model parameters, such as the acoustic efficiency and the jet reference length, could drastically improve the accuracy of the prediction.

B. Hybrid Empirical/Computational Aeroacoustics Prediction

This subsection is focused on the main goal of the present work: to take into account the noise scattering effects due to the mean flow refraction and the multiple wave reflections and diffractions from solid obstacles and edges using the computation of elementary source fields.

The mean flow has been computed using the CFD software FLUENT by solving RANS equations with a Spalart–Allmaras turbulence model and wall functions. The automatic mesh refinement capabilities have been exploited, starting from a tetrahedral mesh. In a previous closely related work [29], the overexpanded jet plume under real liftoff conditions was used as mean flow in the CAA simulation. However, the presence of the shock cells was responsible for an excessively stiff behavior of the hybrid empirical/CAA model, resulting in irregular convoluted noise spectra. In the present work, a jet plume under the equivalent fully expanded conditions is computed and used in the CAA simulation. This choice is motivated by two considerations: 1) the presence of the shock cells, which is crucial in the noise generation process, is accounted for by the

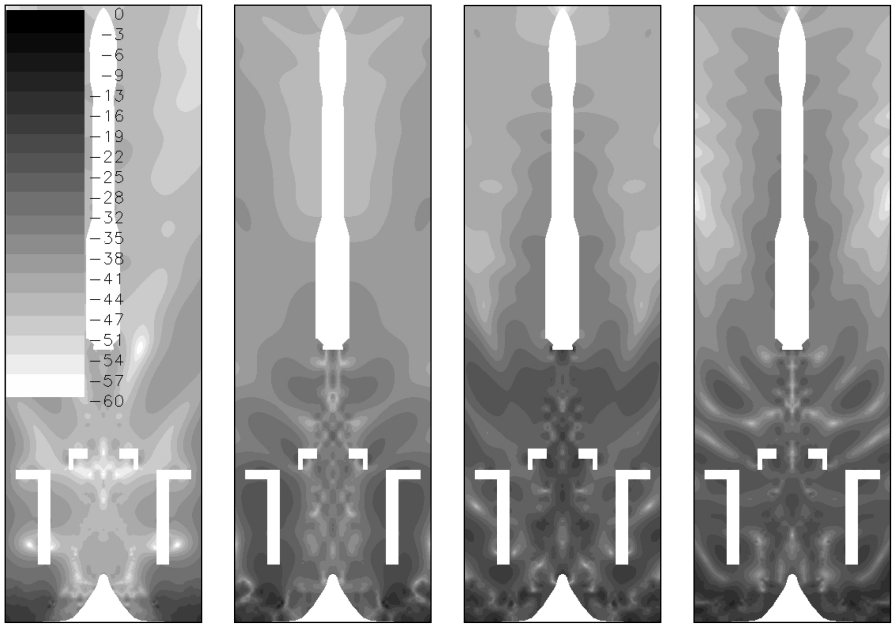

a) 32 Hz b) 40 Hz c) 50 Hz d) 63 Hz

e) 80 Hz f) 100 Hz g) 125 Hz h) 160 Hz

Fig. 19 One-third octave bands SPL contour plots from band 15 (32 Hz) to 22 (160 Hz) computed by means of the hybrid empirical/CAA rocket noise model. A reference value has been subtracted to the plotted levels.

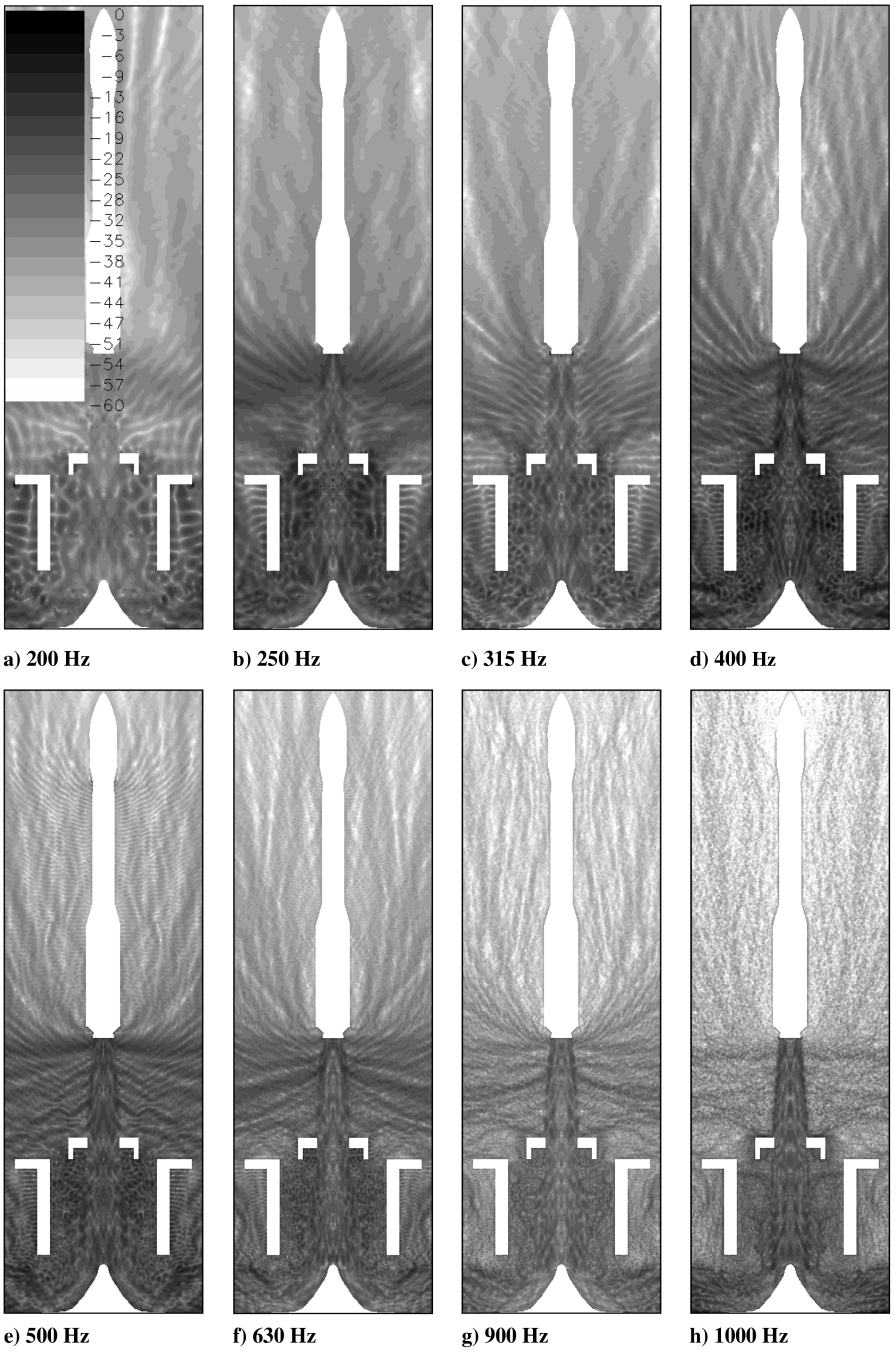

Fig. 20 One-third octave bands SPL contour plots from band 23 (200 Hz) to 30 (1000 Hz) computed by means of the hybrid empirical/CAA rocket noise model. A reference value has been subtracted to the plotted levels.

empirical source strength distribution along the jet center line; and 2) the reliability of the employed wave model is not guaranteed in the presence of discontinuities in the mean flowfield. Contour levels of the normalized velocity magnitude are plotted in Fig. 16b. The jet exhaust Mach number, temperature, and Reynolds number, based on the nozzle diameter, are about 3.5, 1700 K, and 7×10^7, respectively.

CAA computations are carried out by partitioning the multi-frequency analysis among several processors of the hybrid parallel-vectorial supercomputer NEC-SX9. A frequency range of 25–1000 Hz is covered, regardless the applicability limit $f \gtrsim 120$ Hz of the employed wave model obtained in Sec. V.A. For the highest frequency run, the memory occupation peak is about 20 GB and the amount of CPU time for all processors is about 780 h.

Figure 18 shows contour plots on the plane $z = 0$ of the real part of the acoustic potential field at different frequencies generated by the fifteenth Dirac source in the jet plume, which is very close to the edge of the jet deflector (see Fig. 16b). To enhance the graphical quality,

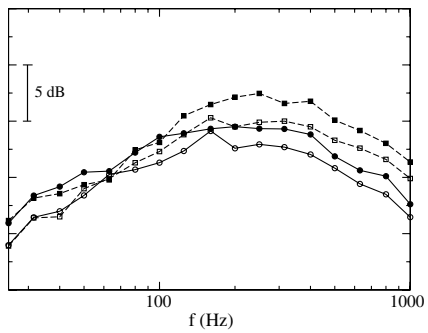

Fig. 21 Vega launcher one-third octave bands SPL. Comparison between experimental data (empty symbols) and hybrid empirical/CAA predictions (filled symbols). Microphone 1: solid lines and circles, microphone 2: dashed lines and squares.

the logarithmic quantity $\log(|Re(\phi)|)\mathrm{sgn}(Re(\phi))$ has been plotted. Two features can be immediately observed: the unsymmetrical wave diffraction patterns and the refraction effects in the jet plume. At certain frequencies, the rhombus texture due to the interaction of characteristic lines are very evident in the jet plume. An interesting behavior has been observed by examining some field animation: the wave fronts from some jet sources, through successive reflections on the walls of the pad cavity, are backinjected into the plume. This

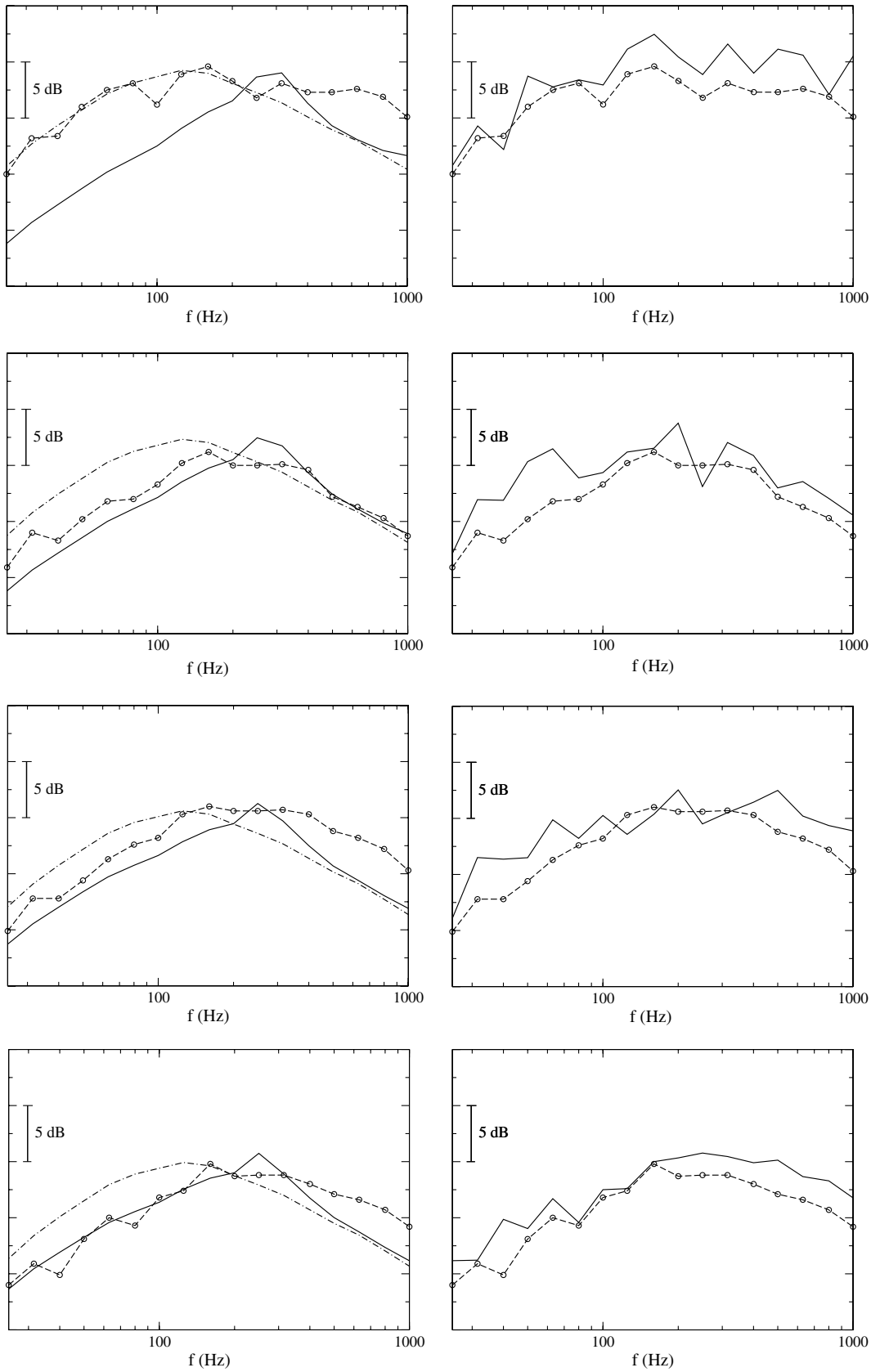

Fig. 22 Vega launcher one-third octave bands SPL for microphones 3–6. Comparison between experimental data (dashed lines with symbols), with Eldred's model results in the left column, and hybrid empirical/CAA model results in the right column. First model: solid lines, second model: dashed lines.

mechanism could promote some feedback loop process, thus enhancing the sound generation at certain frequencies. No experimental evidence of such a mechanism is, however, available. The same backward reflection mechanism is responsible for the noise diffraction at the nozzle edge that can be clearly observed at certain frequencies.

Figures 19 and 20 show the SPL contour plots on the plane $z = 0$ at frequency values corresponding to bands 15–30. A common reference level has been subtracted from all the plotted levels. The analysis of the relative levels at the various frequencies reveals that, at lower frequencies, a confinement effect takes place in the launch pad semiclosed cavity. Conversely, at higher frequencies, the acoustic field is almost uniformly diffused. A direct consequence of this effect could be that the noise levels computed at the fairing level are lower than those provided by a free-field propagation model at lower frequencies. This seems to be confirmed by the noise spectra plotted in Fig. 21.

Figure 21 shows a comparison of the experimental SPL spectra measured at the launcher fairing level and the hybrid empirical/CAA results. It is worthwhile to notice that the peak frequency is predicted quite well and that the level difference between the fairing and free-field microphones increases with frequency. Although the hybrid empirical/CAA method is based on the same source distribution employed by the second variant of Eldred's model, these features are not observed in the results plotted in Fig. 17c. Therefore, we can suppose that, as already pointed out, the global effect due to the launch pad is that of reducing the far-field noise levels at lower frequencies, thus resulting in a higher maximum noise frequency. Finally, we observe that both the fairing and free-field levels are overestimated by 2–3 dB throughout the overall frequency range.

Finally, the noise spectra at other flash-mounted microphones are plotted in Fig. 22. Comparing the measurements with the empirical prediction shows that the predicted spectra at the different locations are practically the same, with a level shift due to the different distance from the jet plume. As already observed in Fig. 17, the second variant of Eldred's model tends to underestimate the maximum noise frequency. This behavior seems to be partially cured by the hybrid empirical/CAA method. Furthermore, we can observe that the empirical/CAA spectra are significantly affected by the microphone location and that the spectral behavior is smoother at higher distances from the jet plume. In other words, the noise interference effects due to the multiple wave reflections tend to vanish away from the launch pad. A similar but less pronounced behavior can be observed in the experimental data. We can therefore affirm that the hybrid empirical/CAA model reproduces in a better way the physics of the noise propagation phenomenon.

The dispersion of the spectral noise levels is due to an excessive sensitivity of the convoluted acoustic fields to wave interference phenomena in the presence of a discrete source distribution. On the other hand, the semi-empirical source distribution, which is the same as the one for an undeflected jet, cannot account for all the noise generation mechanisms occurring in the deflected plume issuing from a solid rocket motor. As a consequence, in the absence of a refined noise source distribution, it is practically impossible to improve the present hybrid empirical/CAA methodology. This lack of description is a clear limitation in the use of the methodology as a predictive tool, but will not prevent the development of a noise source localization methodology, which is the final aim of the ongoing work. The core of a noise source localization method, in fact, is the correct description of the noise diffraction phenomena, which seem to be reproduced well by the present method.

As a final remark, we can state that no influence of the physical unreliability of the employed wave model at low frequency has been observed. This is probably due to the fact that the main effect of a wrong treatment of the mean flow refraction effects is to be found in a bad prediction of the noise directivity. Indeed, because most of the noise generation occurs in the launch pad cavity, the acoustic energy is redistributed in the field, resulting in favorable agreements with the external measurements.

VI. Conclusions

The noise environment generated by the jet plume of a space launcher at liftoff has been computed numerically. The main outcomes of the present work are 1) the validation of an empirical rocket noise model for the prediction of the sound pressure levels generated by the first-stage solid rocket motor of the Vega launch vehicle, and 2) the development of a hybrid empirical/CAA method based on the computation of a numerical Green's function for the whole launch system and realistic jet stream conditions, and further convolution with empirical values of the source magnitude along the jet plume. A tuning of the empirical model is required to improve the accuracy of the prediction, especially for the first variant of Eldred's model. The hybrid empirical/CAA prediction could reduce some discrepancies between measurement and predictions due to the wave reflections on the pad and the launcher surface. Some evidence of such a potentiality of the method has been observed: the lower frequency noise levels are reduced by the hybrid approach, resulting in a better prediction of the maximum noise frequency. In the future research, an inverse method for the jet source localization and noise cross correlation will be developed. This method will be based on the combined use of CAA propagation results to provide the functional basis for the inversion method and RANS simulations to provide a more realistic relative acoustic power distribution along the jet line.

Acknowledgments

The financial support of the Italian Space Agency for the present research and the management staff of the CAST project are acknowledged. The authors are also grateful to Roberto Mella of CIRA Informatic Systems Laboratory for his kind support for the present computational activity.

References

[1] Freund, J. B., "Noise Sources in a Low-Reynolds-Number Turbulent Jet at Mach 0.9," *Journal of Fluid Mechanics*, Vol. 438, 2001, pp. 277–305.doi:10.1017/S0022112001004414

[2] Uzun, A., Blaisdell, G. A., and Lyrintzis, A. S., "Impact of Subgrid-Scale Models on Jet Turbulence and Noise," *AIAA Journal*, Vol. 44, No. 6, 2006, pp. 1365–1368. doi:10.2514/1.9608

[3] Colonius, T., Lele, S. K., and Moin, P., "Sound Generation in a Mixing Layer," *Journal of Fluid Mechanics*, Vol. 330, 1997, pp. 375–409. doi:10.1017/S0022112096003928

[4] Bogey, C., Bailly, C., and Juvé, D., "Computation of Flow Noise Using Source Terms in Linearized Euler's Equations," *AIAA Journal*, Vol. 40, No. 2, 2002, pp. 235–243. doi:10.2514/2.1665

[5] Berland, J., Bogey, C., and Bailly, C., "Large Eddy Simulation of Screech Tone Generation in a Planar Underexpanded Jet," AIAA Paper 2006-2496, 2006.

[6] Bodony, D., Jaiyoung, J. R., and Lele, S. K., "Investigating Broadband Shock-Associated Noise of Axisymmetric Jets Using Large-Eddy Simulation," AIAA Paper 2006-2495, May 2006.

[7] Béchara, W., Bailly, C., and Candel, P. L. S., "Stochastic Approach to Noise Modeling for Free Turbulent Flows," *AIAA Journal*, Vol. 32, No. 3, 1994, pp. 455–464. doi:10.2514/3.12008

[8] Morris, P. J., and Farrasat, F., "Acoustic Analogy and Alternative Theories for Jet Noise Prediction," *AIAA Journal*, Vol. 40, No. 4, 2002, pp. 671–680. doi:10.2514/2.1699

[9] Khavaran, A., and Bridges, J., "Modelling of Turbulence Generated Noise in Jets," AIAA Paper 2004-2983, 2004.

[10] Eldred, K. M., "Acoustic Loads Generated by the Propulsion System," NASA SP-8072, June 1971.

[11] Candel, S., "Analysis of the Sound Field Radiated by the Ariane Launch Vehicle During Lift-Off," *La Recherche Aerospatiale: Bulletin Bimestriel de l'Office National d'Etudes et de Recherches Aerospatiales*, No. 1983-6, 1971, pp. 17–33.

[12] Varnier, J., "Experimental Study and Simulation of Rocket Engine Freejet Noise," *AIAA Journal*, Vol. 39, No. 10, 2001, pp. 1851–1859. doi:10.2514/2.1199

[13] Varnier, J., and Raguenet, W., "Experimental Characterization of the Sound Power Radiated by Impinging Supersonic Jets," *AIAA Journal*,

Vol. 40, No. 5, May 2002, pp. 825–831.
doi:10.2514/2.1746
[14] Varnier, J., "Simplified Approach of Jet Aerodynamics with a View to Acoustics," *AIAA Journal*, Vol. 44, No. 7, July 2006, pp. 1690–1694.
doi:10.2514/1.5087
[15] Campos, E., "Prediction of Noise from Rocket Engines," AIAA Paper 2005-2837, May 2005.
[16] Gély, D., Elias, G., Mascanzoni, F., and Foulon, H., "Experimental Acoustic Characterization of the Vega Launch Vehicle at Lift-Off," *6th International Symposium on Launchers Technologies*, Centre National d'Etudes Spatiales, Paris, Nov. 2005.
[17] Mascanzoni, F., and Contini, C., "The Acoustic Environment of the Vega LV at Lift-Off: the BEAT Acoustic Experimental Test Facility," *6th International Symposium on Launchers Technologies*, Centre National d'Etudes Spatiales, Paris, Nov. 2005.
[18] Ffowcs-Williams, J. E., "The Noise from Turbulence Convected at High Speed", *Proceedings of the Royal Society of London A*, Vol. 255, 1963, pp. 469–503.
doi:10.1098/rsta.1963.0010
[19] Sutherland, L. C., "Progress and Problems in Rocket Noise Prediction for Ground Facilities," AIAA Paper 93-4383, Oct. 1993.
[20] Di Francescantonio, P., and Casalino, D., "Green's Function Discretization Scheme for Sound Propagation in Nonuniform Flows," *AIAA Journal*, Vol. 37, No. 10, 1999, pp. 1161–1172.
doi:10.2514/2.609
[21] Casalino, D., Roger, M., and Jacob, M., "Prediction of Sound Propagation in Ducted Potential Flows Using Green's Function Discretization," *AIAA Journal*, Vol. 42, No. 4, 2004, pp. 736–744.
doi:10.2514/1.1315
[22] Casalino, D., and Genito, M., "Turbofan Aft Noise Predictions Based on the Lilley's Wave Model," *AIAA Journal*, Vol. 46, No. 1, 2008, pp. 84–93.
doi:10.2514/1.32046
[23] Casalino, D., Di Francescantonio, P., and Druon, Y., "GFD Predictions of Fan Noise Propagation," AIAA Paper 2004-2989, May 2004.
[24] Pierce, A. D., "Wave Equation for Sound in Fluids with Unsteady Inhomogeneous Flow," *Journal of the Acoustical Society of America*, Vol. 87, No. 6, 1990, pp. 2292–2299.
doi:10.1121/1.399073
[25] Pridmore-Brown, D. C., "Sound Propagation in a Fluid Flowing Through an Attenuating Duct," *Journal of Fluid Mechanics*, Vol. 4, 1958, pp. 393–406.
doi:10.1017/S0022112058000537
[26] Lilley, G. M., "On the Noise from Jets," AGARD CP-131, 1974.
[27] Casalino, D., and Bodony, D., "Green's Function Discretization of Pridmore-Brown Wave Operator," *Proceedings of the Summer Program 2006*, Center for Turbulence Research, Stanford, CA, 2006, pp. 547–558.
[28] Casalino, D., Genito, M., and Visingardi, A., "Numerical Analysis of Airframe Noise Scattering Effects in Tilt-Rotor Systems," *AIAA Journal*, Vol. 45, No. 4, 2007, pp. 751–759.
doi:10.2514/1.24605
[29] Casalino, D., Barbarino, M., Genito, M., and Ferrara, V., "Improved Empirical Methods for Rocket Noise Prediction through CAA Computation of Elementary Source Fields," AIAA Paper 2008-2939, May 2008.

C. Bailly
Associate Editor